ELSEVIER

https://doi.org/10.1016/j.ultrasmedbio.2019.06.412

● *Original Contribution*

RESOLUTION OF MURINE TOXIC HEPATIC INJURY QUANTIFIED WITH ULTRASOUND ENTROPY METRICS

JON N. MARSH,[*] KEVIN M. KORENBLAT,[†] TA-CHIANG LIU,[‡]
JOHN E. MCCARTHY,[§] and SAMUEL A. WICKLINE[¶]

[*] Department of Immunology & Pathology, Washington University School of Medicine, St. Louis, Missouri, USA; [†] Department of Internal Medicine—Gastroenterology, Washington University School of Medicine, St. Louis, Missouri, USA; [‡] Department of Anatomic & Molecular Pathology, Washington University School of Medicine, St. Louis, Missouri, USA; [§] Department of Mathematics and Statistics, Washington University, St. Louis, Missouri, USA; and [¶] University of South Florida Health Heart Institute, Morsani School of Medicine, Tampa, Florida, USA

Abstract—Image-based classification of liver disease generally lacks specificity for distinguishing between acute, resolvable injury and chronic irreversible injury. We propose that ultrasound radiofrequency data acquired *in vivo* from livers subjected to toxic drug injury can be analyzed with information theoretic detectors to derive entropy metrics, which classify a statistical distribution of pathologic scatterers that dissipate over time as livers heal. Here we exposed 38 C57BL/6 mice to carbon tetrachloride to cause liver damage, and imaged livers *in vivo* 1, 4, 8, 12 and 18 d after exposure with a broadband 15-MHz probe. Selected entropy metrics manifested monotonic recovery to normal values over time as livers healed, and were correlated directly with progressive restoration of liver architecture by histologic assessment ($r^2 \geq 0.95$, $p < 0.004$). Thus, recovery of normal liver microarchitecture after toxic exposure can be delineated sensitively with entropy metrics. (E-mail: wicklines@aol.com) © 2019 World Federation for Ultrasound in Medicine & Biology. All rights reserved.

Key Words: Liver toxicity, Liver recovery, Ultrasound, Entropy, Tissue characterization, Carbon tetrachloride, Quantitative ultrasound.

INTRODUCTION

Liver injury is a known complication of numerous medications that can initiate an injury that spontaneously resolves or, alternatively, an injury that proceeds to either acute liver failure (ALF) or chronic liver disease including cirrhosis (Fisher et al. 2015). Indeed, drug-induced liver injury (DILI) is the leading cause of ALF in the United States, accounting for more cases of ALF than all other etiologies combined including viral hepatitis (Habib and Shaikh 2017; Lee 2013). Though many cases of DILI recover after cessation of the offending agent, those that result in a more severe and non-resolving injury may require rescue with organ transplantation. The use of imaging (magnetic resonance imaging, ultrasound, computed tomography) is common in the evaluation of liver disease but is generally inadequate for ascertaining the nature and severity of the injury and for distinguishing acute from chronic injury (Romero et al. 2014).

Robust and objective methods for characterizing hepatic tissue in the setting of liver injury are limited. Liver biopsy is the most direct method although it is subject to sampling error, is invasive and is not uniformly available. The recent development of various forms of elastography implemented in both magnetic resonance and ultrasound platforms is restricted to the assessment of advanced degrees of fibrosis (Friedrich-Rust et al. 2016). A technology that merges non-invasive imaging with quantitative tissue characterization would provide a novel approach to the evaluation and management of diseases of the liver and other vital organs.

Here we propose to investigate the application of information theoretic detectors (ITDs) to ultrasound data for delineation of liver damage after DILI, and to determine if recovery can be tracked over time after removal of an offending toxin. ITDs constitute a class of mathematical operators that utilize unprocessed radiofrequency (RF) data as input to generate a set of entropy metrics that reveal pathologic alterations in acoustic backscatter from damaged tissues. We have used this approach previously to

Address correspondence to: Samuel A. Wickline, 12901 Bruce B. Downs Boulevard, MDC 36, Tampa, FL 33612, USA. E-mail: wicklines@aol.com

sensitively detect cancer angiogenesis and delineate responses to therapeutic agents in cancer and muscular dystrophy (Hughes et al. 2006, 2007b, 2009a, 2009b, 2011, 2013, 2015), and now seek to apply it to acute hepatic damage in rabbits caused by the classic hepatotoxin carbon tetrachloride (CCl_4). In particular, we are interested in determining how well-selected entropy metrics derived from ultrasound image data might map the temporal evolution of hepatic injury after drug exposure, which could be applicable to quantification of liver damage for any form of acute liver injury.

METHODS

Entropy measures

In general, entropy describes the statistical distribution of amplitude in the backscattered ultrasound RF wave train; traditional ultrasound analysis instead uses the absolute magnitude of backscatter or other related measures such as integrated backscatter (Hughes 1994). Entropy is most commonly computed *via* the histogram of input data values for discretely sampled waveforms or an estimation of the density function in the case of continuous inputs. As such, the entropy associated with some finite region of interest (ROI) might differ for two dissimilar types of tissue that may have equivalent average backscatter magnitudes or envelopes. Thus, entropy metrics may represent additional useful descriptors of the local structure created by scatterers within a volume of tissue.

Entropy is used to detect changes in the homogeneity of the tissue. This is a complex high-dimensional pattern, and an entropy descriptor must reduce it to a single number. Although there is strong experimental support that the entropy descriptors provide more robust descriptors of pathology or flaws in noisy environments than do conventional energy-based measures (Hughes et al. 2006, 2007b, 2009b), it is still unknown which particular descriptor might be optimal for any particular purpose. Moreover, we propose that the use of a set of different entropy descriptors to process ultrasound waveforms might offer a more objective and robust demonstration of the capability of entropy metrics than would a single selected entropy. The algorithms were applied to 32-point segments of each waveform extracted in sliding-boxcar fashion, either through each segment's histogram or from the continuous approximation to its time-domain representation *via* a smoothing spline (Fig. 1). Here we briefly review the definition of each metric and how they were computed.

Shannon entropy. The Shannon entropy, H_S, is determined from the histogram of values $\{p_i\}_{i=1,\ldots,N}$ in the digitized waveform (where N is the number of discrete digitizer levels) and is defined as (Hughes et al. 2005b, 2006)
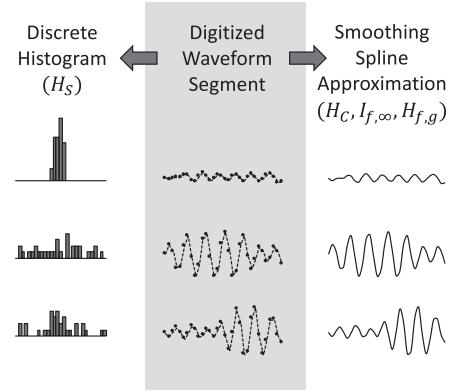

Fig. 1. Discretely digitized waveform segments (three examples are shown in the center column) were used to derive either a histogram for computation of Shannon entropy (left column) or a continuous time-domain approximation using a smoothing spline for computation of continuous, Rényi and joint entropies *via* computation of the density function (right column).

$$H_S = -\sum_{i=1}^{N} p_i \log[p_i], \text{ where } 0 \ \ln[0] := 0 \qquad (1)$$

In the results presented below, 256-bin histograms were used with maximum/minimum values corresponding to the maximum amplitude setting of the digitizer.

Continuous entropy. The finite part of the Shannon entropy in the limit of infinitely small sampling intervals and digitization levels (Hughes 1994; Hughes et al. 2007b) is given by

$$H_C = -\int w(y) \log[w(y)] dy \qquad (2)$$

where $w(y)$ is the probability density function (PDF) of the waveform $y = f(t)$ (note that we have changed the sign convention of this value relative to the references listed above to maintain consistency with the definition of the Shannon entropy). Because the PDF of a continuous, smoothly varying oscillating waveform can have multiple singularities and is therefore non-trivial to compute, we make use of an alternative formulation derived from the time-domain function through the relation

$$H_C = \int \log[f'_\uparrow(t)] dt \qquad (3)$$

where $f_\uparrow(t)$ denotes the increasing rearrangement of $f(t)$ (Hughes et al. 2007b). In the case of discretely sampled waveforms, this may be approximated quickly by sorting the input waveform (Hughes et al. 2007b). It should, however, be noted that the increasing rearrangement of a sufficiently long, discretely digitized, oscillating signal will likely have regions of zero slope, leading to

singularities in this approximation. For the present results, waveform segments were resampled using cubic spline interpolation at points between the original sampling times to effectively remove artifacts associated with digitization before applying the approximation. This procedure yields results consistent with the PDF approach of eqn (2) while permitting efficient computation (Hughes et al. 2011).

Singular Rényi entropy. The Rényi entropy is a generalization of the Shannon entropy and is defined as

$$I_f(r) = \frac{1}{1-r} \log \left[\int w_f(y)^r dy \right] \quad (4)$$

where r is an adjustable parameter. In the limit as $r \to 1$, we get $I_f(r) \to H_C$. Prior work has revealed that this quantity exhibits sensitivity to small changes in scattering parameters that is enhanced in the limit $r \to 2^-$ (Hughes et al. 2009b). It is important to note that the density function $w_f(y)$ of a continuous, smoothly varying oscillating waveform, $f(t)$ yields an expression for $I_f(r)$ that is undefined when $r \geq 2$ because of the singularities in $w_f(y)$. However, it has been found that the asymptotic form of $I_f(r)$ as $r \to 2$ from below can be given by

$$I_{f,\infty} = -\log \left[\sum_{\{t_k | f'(t_k)=0\}} \frac{1}{|f''(t_k)|} \right] \quad (5)$$

where the t_k are the zeroes of the derivative of $f(t)$ (again note the change in sign convention) (Hughes et al. 2009a). In the present study, an optimal smoothing spline (Reinsch 1967) was used to compute the required first and second derivatives of the input waveform segment and reduce the impact of noise on the computation of derivatives needed for computation of $I_{f,\infty}$ (Hughes et al. 2011).

Joint entropy. The joint entropy of two functions $f(t)$ and $g(t)$ having associated joint density $w(x, y)$ is given by

$$H(f, g) = -\iint w(x, y) \log[w(x, y)] \, dx \, dy \quad (6)$$

As with the continuous and singular Rényi entropies, the density function $w(x, y)$ for the types of "well-behaved" time-domain input functions considered here renders this equation not well defined, because the support of $w(x, y)$ is one-dimensional. It has, however, been found that the following relationship holds true (note change in sign convention) (Hughes et al. 2013):

$$H_{f,g} \equiv \frac{1}{2} \int dt \frac{\min\left[\left|f'(t)\right|, \left|g'(t)\right| \right]}{\max\left[\left|f'(t)\right|, \left|g'(t)\right| \right]}$$
$$+ \int dt \log\left[\left| \max\left[\left|f'(t)\right|, \left|g'(t)\right| \right] \right| \right] \quad (7)$$

In this case we again made use of an optimal smoothing spline fit to each waveform segment to obtain the required first derivatives of the functions $f(t)$ and $g(t)$. As described above, RF waveform segments are assigned to $f(t)$. The choice for the reference waveform $g(t)$ is an additional degree of freedom, which in this case was derived from the reflection of the imaging system's interrogating pulse from a planar reflector (Hughes et al. 2015).

Treatment

All animal experiments used in this study were conducted in an ethical and humane fashion governed by protocols approved by the Institutional Animal Care and Use Committee of Washington University. Normal mice (C57 BL/6 J, The Jackson Laboratory, Bar Harbor, ME, USA) at 12 wk of age were administered intraperitoneal injections of CCl_4 twice weekly for 4 wk. CCl_4 (Sigma-Aldrich, St. Louis, MO, USA) was prepared in a vehicle of sunflower oil and administered at a dose of 0.4 μL/g weight. The mice were divided into groups according to the interval between the final injection and data acquisition/sacrifice: 1 d (n = 9), 4 d (n = 8), 8 d (n = 9), 12 d (n = 6) or 18 d (n = 6). Sample numbers were larger for the 1-, 4- and 8-d recovery groups because of inclusion of additional mice from a smaller, identically prepared pilot study (not previously published) conducted to determine project feasibility. A separate group of control mice (n = 5) were left untreated. After ultrasound data acquisition (described below), each mouse was euthanized by cervical dislocation, and thoracotomy/laparotomy was performed. While the heart was still beating, physiologic saline solution was infused continuously into the left ventricle until the liver turned pale and stopped changing color. The liver was then excised, immersed in optimal cutting temperature compound (Tissue-Plus, Fisher Scientific, Waltham, MA, USA) and frozen for histologic processing and biochemical collagen assay.

Data acquisition

At selected intervals during recovery after liver injury, mice were lightly anesthetized with 1.5% isoflurane before depilation of the abdomen. Each mouse was placed semi-supine on a heated platform and maintained on isoflurane anesthetic. Pre-warmed ultrasound gel was liberally applied to the skin above the liver. A handheld

15-MHz linear array (Spark Imaging System, Ardent Sound, Inc., Mesa, AZ, USA) was used to acquire transcutaneous images of the liver. Before the start of the study, optimal system settings for transmit power (-3 dB), receive gain (0.0 dB) and focal zones (single focal zone at position 4, with 30-mm field of view) were selected to provide the best view of the right medial lobe of the liver, while ensuring RF signal output levels were within the dynamic range of the digitizer. These settings remained constant for all time points and all mice to maintain consistency between measurements

The imaging system was modified to output beamformed raw RF data and associated line and frame trigger signals. The RF output for each A-line was digitized to 12 bits at a sampling rate of 66.67 MHz with an externally clocked Peripheral Component Interface (PCI)-based digitizer card (GaGe Compuscope 12400, DynamicSignals LLC, Lockport, IL, USA) using custom software written in LabVIEW (National Instruments Corp., Austin, TX, USA). A 3-s cine loop (200 frames, with 256 lines per frame and 2048 points per A-line) was acquired in this manner as the probe was manually positioned over the abdomen proximal to the right medial lobe of the liver, and the resulting data were stored for offline processing.

Data processing

Data were processed using custom plugins written in Java for the open-source image-editing package ImageJ (Schneider et al. 2012). Data processing was performed using 32-point (0.48-μs, equivalent to 0.37-mm) moving-window analysis, in which a specific ITD (H_S, H_C, $I_{f,\infty}$, or $H_{f,g}$) was computed for each window segment. The window segment length was selected based on the approximate length of the transducer output pulse, and corresponded to approximately 7 cycles at the transducer center frequency. Each computed value was mapped to the center point of the original segment. The fully processed data set was mapped to gray scale, and the resulting image scaled to the appropriate aspect ratio.

For each mouse, a representative frame revealing a portion of the right liver lobe (having uniform texture and free from major ducts or vessels) was selected from the conventional ultrasound cine loop. Figure 2 illustrates grayscale rendering of an example frame using conventional processing (*i.e.,* log of signal magnitude) and entropy processing with each of the ITDs, from an untreated mouse (top row) and a mouse exposed for 4 wk to CCl_4 (bottom row). A 15-mm^2 circular ROI was positioned within the central portion of the right medial lobe approximately 3 mm below the skin (see Fig. 3 for illustration). The same ROI was applied to images generated with each of the previously described quantities, and the mean values within the ROIs were computed. A two-parameter exponential equation of the form $\Delta H = ae^{bF}$ (where ΔH is an entropy metric's difference from baseline and F is the fibrosis metascore, defined below) was fit to the results as a means of modeling the correlation with liver recovery.

Histology

Frozen liver tissue was sectioned and treated with hematoxylin and eosin (H&E) and picrosirius red stains for visualization of fatty and fibrous components. Slides were imaged at 20 × and large representative areas (*e.g.,* between 6 to 12 contiguous visual fields) were captured and stitched together digitally for subsequent blinded examination by an expert pathologist (T.C.L.). Example H&E fields for control livers and livers exposed to CCl_4 with sequential stages of recovery are provided in Figure 4. Liver sections were graded on a nominal scale for portal fibrosis (0 = none, 1 = thickened basement membrane, 2 = mild periportal fibrosis, 3 = moderate periportal fibrosis, 4 = portal−portal bridging); perivenular fibrosis (0 = none, 1 = thickened basement membrane, 2 = fibrosis extending into parenchyma, 3 = long fibrosis bands extending into parenchyma, 4 = zone 3−zone 3 bridging); cholestasis (0 = none, 1 = mild,
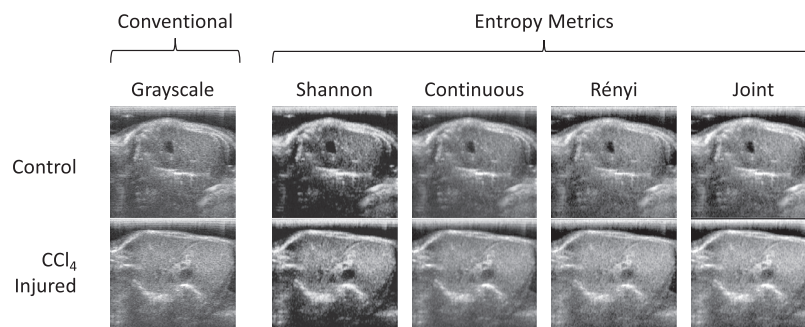

Fig. 2. Grayscale rendering of an example frame using conventional processing (*i.e.,* log of signal magnitude) and entropy processing with each of the information theoretic detectors. Top row: frame for an untreated mouse; bottom row: frame for a mouse exposed to 4 wk of CCl_4.

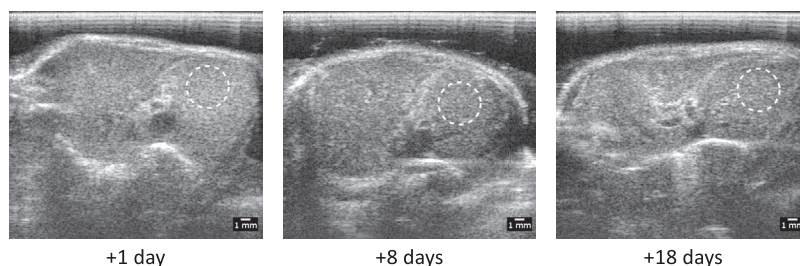|		
+1 day	+8 days	+18 days

Fig. 3. B-Scan view (conventional ultrasound, *i.e.,* log of analytic signal magnitude) of right lobe of example mouse livers after varying lengths of treatment with CCl$_4$. The circular region of interest delineated by the *white dotted line* indicates area from which entropy metrics were extracted.
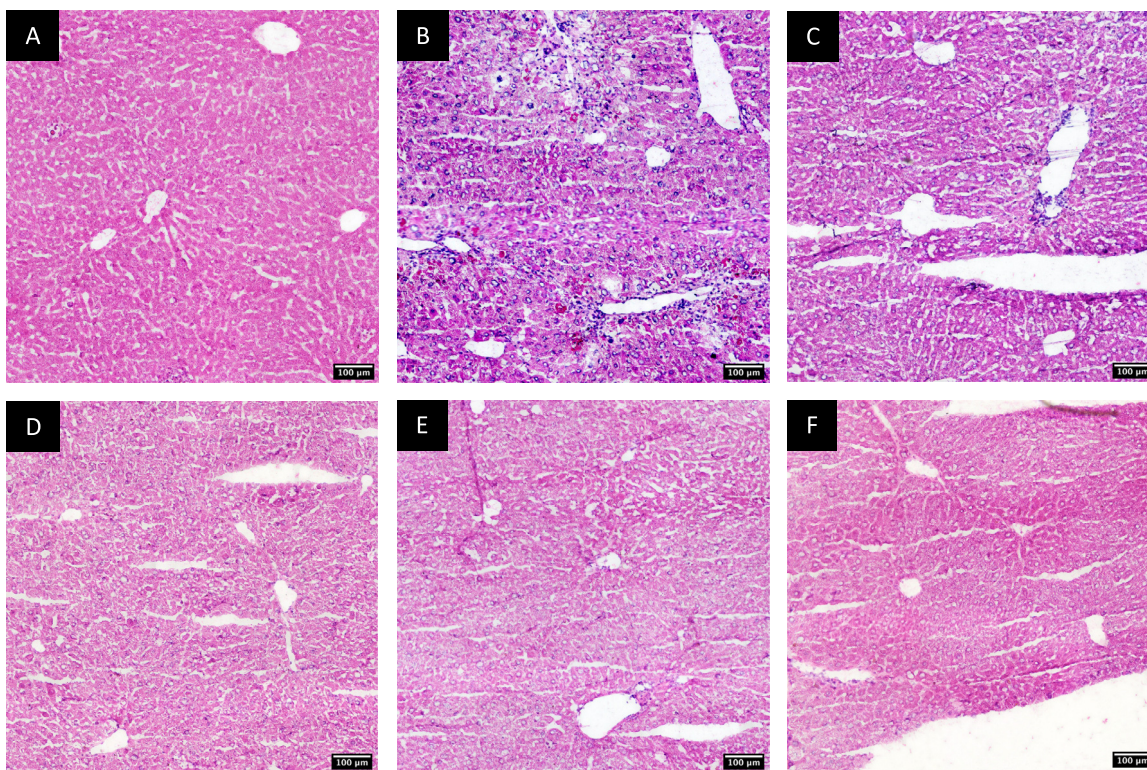

Fig. 4. Example fields of hematoxylin and eosin stains of mouse liver for untreated mice (A) and for mice given CCl$_4$ for 4 wk and left to recover for 1 d (B), 4 d (C), 8 d (D), 12 d (E) and 18 d (F). Bars = 100 μm.

2 = moderate, 3 = severe); and zone 3 chronic inflammation (0 = none, 1 = mild, 2 = moderate, 3 = severe). Area of necrosis also was estimated visually. Steatosis was not graded because no significant fat accumulation was observed in any of the groups.

Liver function and collagen content

Samples of excised liver tissue from each mouse were assayed to determine total liver collagen content (Cedarlane Labs kit, Burlington, NC, USA). Aminotransferases were determined in a subset of mice from the 1-d recovery group and a set of untreated mice (n = 3 for each group).

RESULTS

Histologic analysis revealed substantial changes in liver morphology associated with acute exposure to CCl$_4$, with moderate necrosis (typically ∼20%) and focal fibrosis especially evident in perivenular areas (zone 3). Zone 3 inflammation, fibrosis and cholestasis decreased during the recovery period. To succinctly express the degree of pathology exhibited in the tissue from each mouse, a single metascore was computed by expressing each of the individual pathology grades as a fraction of the maximum value and taking the mean of the resulting normalized scores. The continuously improving liver metascore clearly reflects liver healing
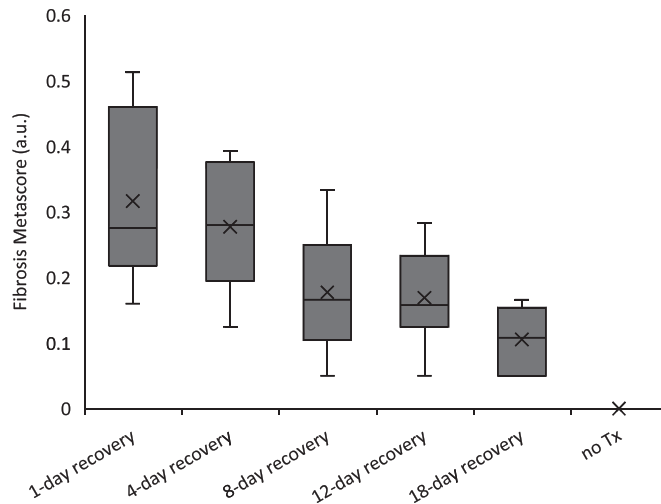
Fig. 5. Fibrosis metascore exhibits continuous improvement with recovery time, although not yet to baseline level at the final observed time point at 18 d.

over time, although recovery to normal values was incomplete within the 18-d recovery time frame of this study (Fig. 5; for all whisker plots, an 'X' symbol marks the mean value, the horizontal line within the box marks the median, the box top and bottom mark the limits of the 75th and 25th percentiles, respectively, and the whiskers mark the extent of the rest of the data. Outliers, defined as lying more than 1.5 times the interquartile range from either end of the box, are plotted as individual points). Elevated liver enzymes for the earliest recovery group (1-d recovery: alanine aminotransferase [ALT] = 1710 $\pm$ 170 U/L, aspartate aminotransferase [AST] = 1020 $\pm$ 5 U/L) further confirmed impaired liver function relative to untreated animals (ALT = 70 $\pm$ 10 U/L, AST = 70 $\pm$ 20 U/L). In contrast, liver collagen content did not exhibit a clear trend over the recovery times (Fig. 6).

Entropy metric mean values likewise exhibited a dependence on recovery time (Fig. 7). Significant differences at the $p < 0.05$ level (unpaired two-tail t-tests) with respect to the untreated cohort were observed at the 1- and 4-d recovery time points. Unlike the fibrosis scores, however, these metrics returned to normal values by the 18-d recovery point. Moreover, all metrics had a monotonic relationship to fibrosis score with a recovery process that fit an exponential model well over the range of data in this study (Fig. 8, Table 1). All entropy metrics behaved similarly, outside of expected differences in magnitude and offset.
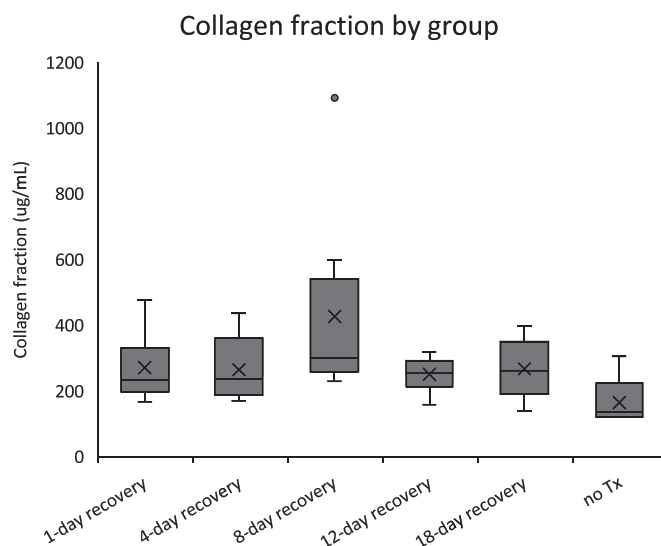

Fig. 6. Collagen fraction (measured by histochemical assay) exhibits no clear trend as a function of recovery time.
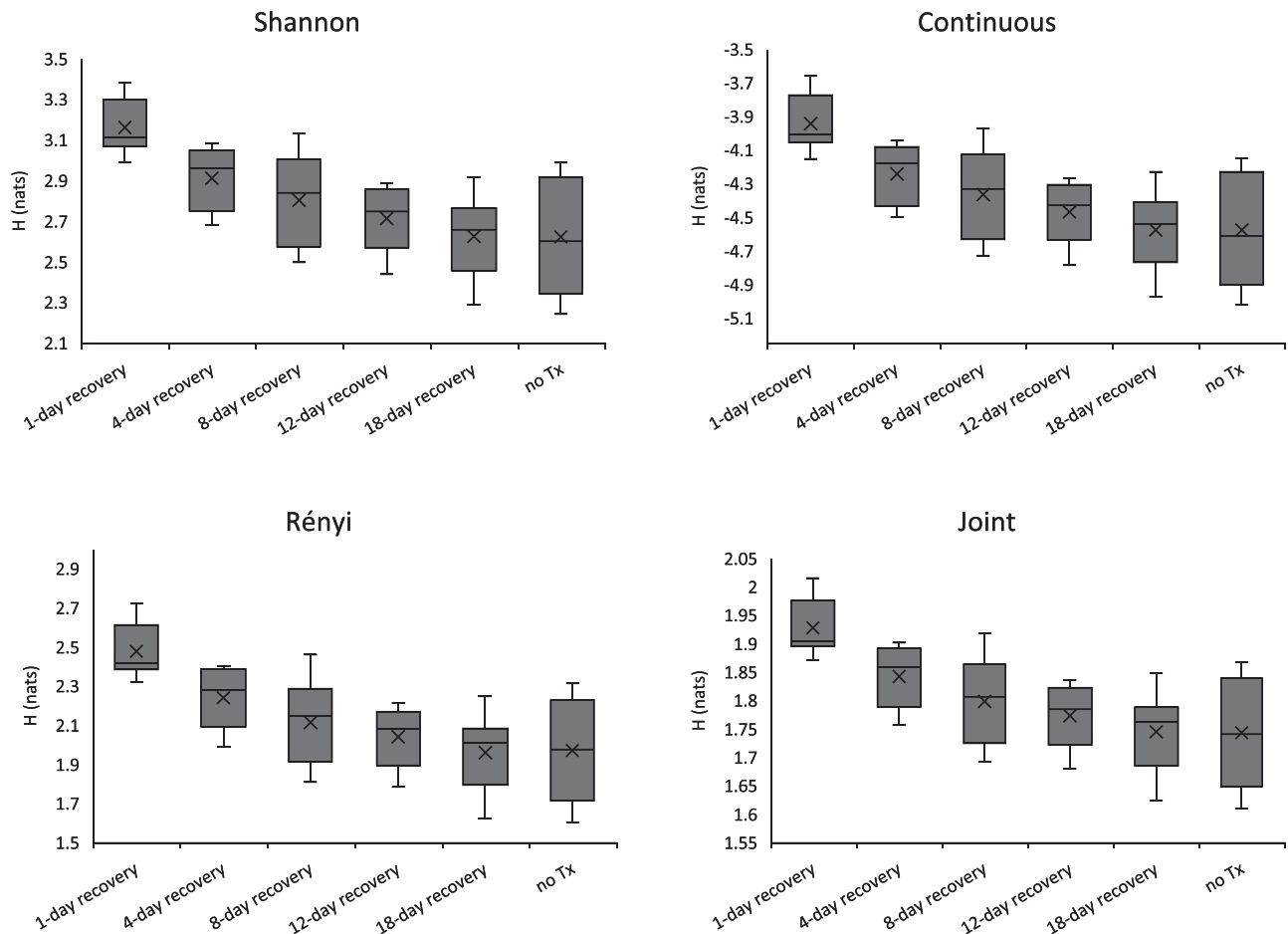
Shannon

Continuous

Rényi

Joint

Fig. 7. Mean entropy values as a function of recovery time. All metrics demonstrate a return to normal values at the 4-wk recovery point.

DISCUSSION

In the present investigation, we acquired radiofrequency ultrasound backscatter waveforms *in vivo* from mouse livers with reversible toxic damage and quantified the natural healing response with the use of sensitive and objective ITD signal processing techniques (Hughes 1994; Hughes et al. 2005b, 2006, 2007b, 2009a, 2009b, 2011, 2013, 2015; Wallace et al. 2007). In general, ITD methods operate by analyzing the statistical distribution of digitized voltage levels from an acoustic signal and are sensitive to diffuse, low-amplitude features of the signal that often are obscured by noise or lost in large specular echoes that can inhibit recognition (Cheng et al. 2009; Hughes 1992, 1993a, 1993b; Hughes et al. 2005b). The relative insensitivity to confounding atypical bright spot scatterers, noise and specular echoes indicates that these features would not dominate the outcome for entropy analysis as they might for measures of the average magnitudes of energy in a windowed region of interest, for example. The family of entropy metrics investigated here all performed similarly

well to depict tissue recovery, suggesting that any or all might be candidates for further evaluation in actual patients with liver diseases.

We have previously reported that ultrasound entropy metrics can detect subtle tissue damage in a number of distinct pathologies. For example, in the mdx mouse, a model of Duchenne muscular dystrophy resulting from a complete lack of the membrane-stabilizing protein dystrophin, entropy metrics were able to differentiate diseased from normal biceps in mdx mice versus non-dystrophic control mice (Hughes et al. 2007b, 2011). Moreover, treatment of mdx mice with corticosteroids elicited improvements in muscle disease that could be sensitively depicted after only 2 wk as a restoration of more normal entropy values. Traditional energy metrics (*e.g.,* "integrated backscatter") proved insensitive for detection of the therapeutic response to steroids in this study. Exceptional sensitivity to weak scattering perfluorocarbon nanoparticles that are molecularly targeted to neovasculature in tumors and injured tissues in animal models *in vivo* has been demonstrated at concentrations
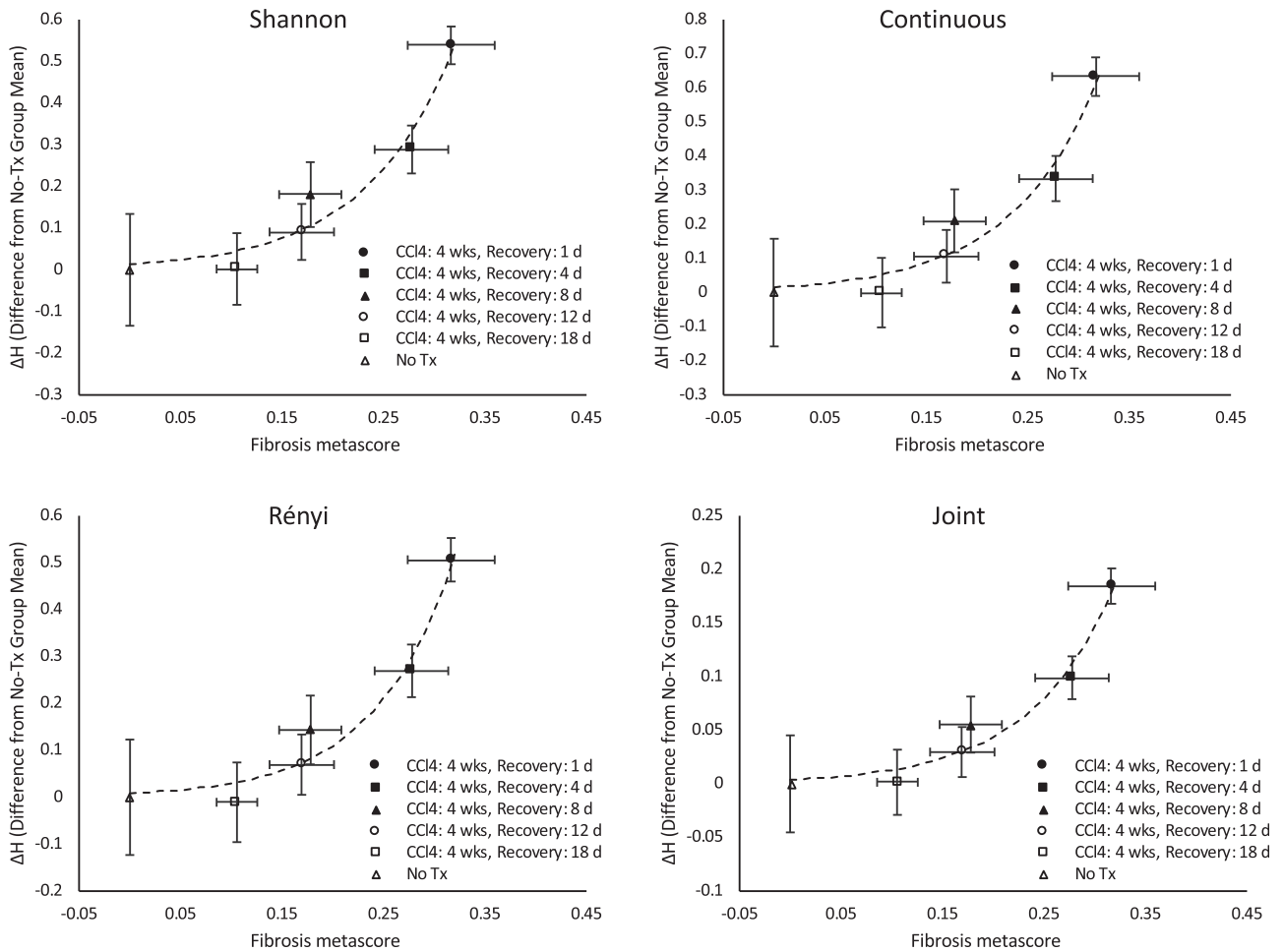
Fig. 8. Difference in mean entropy metrics from baseline (no treatment) exhibits a clear monotonic increase with increasing fibrosis metascore. The *dotted line* indicates the exponential fit to data (see Table 1 for details).

Table 1. Exponential model fit parameters for difference in mean entropy metrics from baseline as a function of fibrosis metascore*

Shannon			Continuous			Rényi			Joint		
a	b	r^2	A	b	r^2	a	b	r^2	a	b	r^2
0.0135	11.53	0.953	0.0152	11.67	0.951	0.0082	12.93	0.966	0.0039	12.06	0.966

* See Figure 7. The exponential model is of the form $\Delta H = ae^{bF}$, where ΔH is the associated entropy metric difference from baseline, and F is the fibrosis metascore.

that are undetectable with conventional methods (Hughes et al. 2006, 2007b, 2009b). In industrial applications, these receivers allow detection of subtle flaws in materials that are obscured by strong specular reflectors, thereby overcoming some of the limitations of more conventional signal processing schemes (Hughes 1994; Hughes et al. 2005b, 2015).

Alternative strategies have been proposed for quantifying and/or staging liver disease processes using ultrasound tissue characterization (Oelze and Mamou 2016). Well-known metrics such as backscatter and attenuation show increased magnitude associated with hepatopathy (Guimond et al. 2007; Lu et al. 1997). Multiparametric combinations of these quantities with other conventional metrics such as speed of sound discriminate fibrosis better than when considered singularly (Bouzitoune et al. 2016). Statistical modeling of the envelope-detected backscatter from liver (Ho et al. 2012; Ma et al. 2016; Owjimehr et al. 2017) has shown promise for evaluating the degree of hepatic fibrosis and steatosis, whereas B-scan texture analysis (Vicas et al. 2011) has proved less useful in the clinic. Recently, photoacoustic techniques have been used utilized

to differentiate healthy and fibrotic livers in a CCl₄ mouse liver injury model (van den Berg et al. 2016).

The recent advent of shear wave ultrasound imaging for quantification of liver fibrosis is a welcome addition to the diagnostic armamentarium of non-invasive imaging; however, this approach requires the use of equipment capable of propagating shear waves transcutaneously into the liver and of simultaneously receiving and processing backscattered compressional waves that are used to register the speed of sound in regions of interest for calculation of an elastic modulus (Barr 2018). The ability to employ conventional clinical imaging platforms would render point-of-care applications more viable as entropy detection now can be done in real time if unprocessed RF data are available (Hughes et al. 2009a).

What is not addressed in this study is the fundamental nature of the scattering elements that are responsible for the basic signal and its progressive recovery over time. Because there is no specific trend in overall liver collagen concentration over time, we do not attribute the observed behavior to gross changes in physical characteristics such as material compressibility or density that would be indicative of resolving fibrosis. However, our blinded pathologic analyses do indicate changes in the organization of collagen over time even if the total amounts of collagen are not changing enough to account for restoration of entropy values. Therefore, we propose that the entropy metrics are sensitive to the specific microscopic organization of disrupted liver tissue elements rather than collagen amount as far as this model of toxic injury is concerned. This notion is entirely consistent with the expectation that entropy metrics more likely represent how scatterers are arranged, in the sense of local information content, rather than their average backscatter cross-section *per se* Whether entropy metrics would be sensitive to collagen formation characteristic of cirrhosis is an interesting question for future study. Other potential mechanisms that could influence entropy metrics include cellular ballooning, hepatocyte necrosis/apoptosis, hemorrhage and inflammatory infiltrates, many of which are represented in our liver metascore metric (Fig. 5) and are topics for further exploration.

In terms of limitations, the present study was performed with an experimental broadband imaging system operating at a nominal center frequency of 15 MHz. Whether the same sensitivities of entropy metrics to liver damage might be obtained at lower frequencies with clinical imaging systems is conjectural, but certainly testable in patients. We have applied entropy imaging and analytical techniques *in vivo* to actual patients with Duchenne muscular dystrophy versus normal control patients using broadband clinical 7-MHz ($\sim$4.5$-$9.5 MHz) ultrasound to reveal clear differences between damaged and normal biceps muscle tissues (Hughes et al. 2007a). These muscles harbor many similarities in altered and disordered cellular and matrix structures as do the damaged livers (edema, fibrosis, cellular damage, *etc.*) indicating that at clinical imaging frequencies, ITDs are sensitive to tissue damage. We also have reported *in vivo* sensitivity to pathologic changes in muscular dystrophy and cancer at frequencies up to 40 MHz, indicating the applicability of entropy metrics over a broad range of frequencies (Hughes et al. 2005a; Wallace et al. 2007). Testing of entropy metrics against well-characterized phantom scattering models for relevant clinical imaging units would be required to ensure equivalent performance of the various platforms.

CONCLUSIONS

We suggest that the entropy metrics derived from conventional longitudinal wave ultrasound RF backscatter data could offer more sensitivity to early changes in liver architecture, whereas shear wave-based readouts appear to be somewhat less sensitive, and conventional spectral tissue characterization metrics (*e.g.,* integrated backscatter, frequency dependence) appear even less sensitive in clinical trials larger than those mentioned above (Audière et al. 2011). With recent algorithmic improvements in entropy computation allowing real-time quantification, the opportunity now exists for porting these procedures to any imaging platform for patient imaging and stand-alone point-of-care analyses.

REFERENCES

Audière S, Angelini ED, Charbit M, Miette V. Evaluation of in vivo liver tissue characterization with spectral RF analysis versus elasticity. Berlin/Heidelberg: Springer; 2011. p. 387–395.

Barr RG. Shear wave liver elastography. Abdom Radiol 2018;43:800–807.

Bouzitoune R, Meziri M, Machado CB, Padilla F, de Pereira WC. Can early hepatic fibrosis stages be discriminated by combining ultrasonic parameters? Ultrasonics 2016;68:120–126.

Cheng YJ, Hughes MS, Marsh JN, Wallace KD, Wickline SA. Shannon entropy can detect myocardial anisotropy without specular echo gating in vitro. J Acoust Soc Am 2009;126:2214.

Fisher K, Vuppalanchi R, Saxena R. Drug-induced liver injury. Arch Pathol Lab Med 2015;139:876–887.

Friedrich-Rust M, Poynard T, Castera L. Critical comparison of elastography methods to assess chronic liver disease. Nat Rev Gastroenterol Hepatol 2016;13:402–411.

Guimond A, Teletin M, Garo E, D'Sa A, Selloum M, Champy MF, Vonesch JL, Monassier L. Quantitative ultrasonic tissue characterization as a new tool for continuous monitoring of chronic liver remodelling in mice. Liver Int 2007;27:854–864.

Habib S, Shaikh OS. drug-induced acute liver failure. Clin Liver Dis 2017;21:151–162.

Ho MC, Lin JJ, Shu YC, Chen CN, Chang KJ, Chang CC, Tsui PH. Using ultrasound Nakagami imaging to assess liver fibrosis in rats. Ultrasonics 2012;52:215–222.

Hughes MS. A comparison of Shannon entropy versus signal energy for acoustic detection ofartificially induced defects in plexiglass. J Acoust Soc Am 1992;91:2272–2275.

Hughes MS. Analysis of digitized waveforms using Shannon entropy. J Acoust Soc Am 1993;93:892–906.

Hughes MS. NDE imaging of flaws using rapid computation of Shannon entropy. Proc IEEE Int Ultrason Symp 1993;697–700.

Hughes MS. Analysis of digitized waveforms using Shannon entropy: II. High−speed algorithms based on Green's functions. J Acoust Soc Am 1994;95:2582–2588.

Hughes M, Marsh JN, Arbeit J, Neumann R, Fuhrhop RW, Lanza GM, Wickline SA. Ultrasonic molecular imaging of primordial angiogenic vessels in rabbit and mouse models with $\alpha v \beta 3$-integrin targeted nanoparticles using information-theoretic signal detection: Results at high frequency and in the clinical diagnostic frequency range. Proc IEEE Int Ultrason Symp 2005;617–620.

Hughes MS, Marsh JN, Hall CS, Savéry D, Lanza GM, Wickline SA. Characterization of digital waveforms using thermodynamic analogs: Applications to detection of materials defects. IEEE Trans Ultrason Ferroelectr Freq Control 2005;52:1555–1564.

Hughes MS, Marsh JN, Zhang H, Woodson AK, Allen JS, Lacy EK, Carradine C, Lanza GM, Wickline SA. Characterization of digital waveforms using thermodynamic analogs: Detection of contrast-targeted tissue in vivo. IEEE Trans Ultrason Ferroelectr Freq Control 2006;53:1609–1616.

Hughes MS, Marsh JN, Wallace KD, Donahue TA, Connolly AM, Lanza GM, Wickline SA. Sensitive ultrasonic detection of dystrophic skeletal muscle in patients with Duchenne muscular dystrophy using an entropy-based signal receiver. Ultrasound Med Biol 2007;33:1236–1243.

Hughes MS, McCarthy JE, Marsh JN, Arbeit JM, Neumann RG, Fuhrhop RW, Wallace KD, Znidersic DR, Maurizi BN, Baldwin SL, Lanza GM, Wickline SA. Properties of an entropy-based signal receiver with an application to ultrasonic molecular imaging. J Acoust Soc Am 2007;121:3542–3557.

Hughes MS, Marsh JN, Arbeit JM, Fuhrhop RW, Wallace KD, Thomas T, Smith J, Agyem K, Lanza GM, Wickline SA, McCarthy JE, Wickerhauser M V. Real-time calculation of a limiting form of the renyi entropy for detection of subtle changes in scattering architecture. Proc IEEE Int Ultrason Symp 2009;2350–2358.

Hughes MS, Marsh JN, Arbeit JM, Neumann RG, Fuhrhop RW, Wallace KD, Thomas L, Smith J, Agyem K, Lanza GM, Wickline SA, McCarthy JE. Application of Renyi entropy for ultrasonic molecular imaging. J Acoust Soc Am 2009;125:3141–3145.

Hughes MS, Marsh JN, Agyem KF, McCarthy JE, Maurizi BN, Wickerhauser MV, Wallace KD, Lanza GM, Wickline SA. Use of smoothing splines for analysis of backscattered ultrasonic waveforms: Application to monitoring of steroid treatment of dystrophic mice. IEEE Trans Ultrason Ferroelectr Freq Control 2011;58:2361–2369.

Hughes MS, McCarthy JE, Marsh JN, Wickline SA. Joint entropy of continuously differentiable ultrasonic waveforms. J Acoust Soc Am 2013;133:283–300.

Hughes MS, McCarthy JE, Bruillard PJ, Marsh JN, Wickline SA. Entropy vs. energy waveform processing: A comparison based on the heat equation. Entropy 2015;17:3518–3551.

Lee WM. Drug-induced acute liver failure. Clin Liver Dis 2013; 17:575–586.

Lu ZF, Zagzebski JA, O'Brien RT, Steinberg H. Ultrasound attenuation and backscatter in the liver during prednisone administration. Ultrasound Med Biol 1997;23:1–8.

Ma HY, Zhou Z, Wu S, Wan YL, Tsui PH. A computer-aided diagnosis scheme for detection of fatty liver in vivo based on ultrasound kurtosis imaging. J Med Syst 2016;40:33.

Oelze ML, Mamou J. Review of quantitative ultrasound: Envelope statistics and backscatter coefficient imaging and contributions to diagnostic ultrasound. IEEE Trans Ultrason Ferroelectr Freq Control 2016;63:336–351.

Owjimehr M, Danyali H, Helfroush MS, Shakibafard A. Staging of fatty liver diseases based on hierarchical classification and feature fusion for back-scan-converted ultrasound images. Ultrason Imaging 2017;39:79–95.

Reinsch CH. Smoothing by spline functions. Numer Math 1967; 10:177–183.

Romero M, Palmer SL, Kahn JA, Ihde L, Lin LM, Kosco A, Shinar R, Ghandforoush A, Chan LS, Petrovic LM, Sher LS, Fong TL. Imaging appearance in acute liver failure: Correlation with clinical and pathology findings. Dig Dis Sci 2014;59:1987–1995.

Schneider CA, Rasband WS, Eliceiri KW. NIH Image to ImageJ: 25 years of image analysis. Nat Methods 2012;9:671–675.

van den Berg PJ, Bansal R, Daoudi K, Steenbergen W, Prakash J. Preclinical detection of liver fibrosis using dual-modality photoacoustic/ultrasound system. Biomed Opt Express 2016;7:5081–5091.

Vicas C, Lupsor M, Badea R, Nedevschi S. Usefulness of textural analysis as a tool for noninvasive liver fibrosis staging. J Med Ultrason 2011;38:105–117.

Wallace KD, Marsh JN, Baldwin SL, Connolly AM, Keeling R, Lanza GM, Wickline SA, Hughes MS. Sensitive ultrasonic delineation of steroid treatment in living dystrophic mice with energy-based and entropy-based radio frequency signal processing. IEEE Trans Ultrason Ferroelectr Freq Control 2007;54:2291–2299.